



**HAL**  
open science

# The potential of marine ferromanganese nodules from Eastern Pacific as recorders of Earth's magnetic field changes during the past 4.7 Myr: a geochronological study by magnetic scanning and authigenic $^{10}\text{Be}/^{9}\text{Be}$ dating

L. Yi, M. Medina-elizalde, G. Kletetschka, H. Yao, Quentin Simon, G. Paterson, D. Bourles, X. Deng, J. Du, H. Qin, et al.

## ► To cite this version:

L. Yi, M. Medina-elizalde, G. Kletetschka, H. Yao, Quentin Simon, et al.. The potential of marine ferromanganese nodules from Eastern Pacific as recorders of Earth's magnetic field changes during the past 4.7 Myr: a geochronological study by magnetic scanning and authigenic  $^{10}\text{Be}/^{9}\text{Be}$  dating. *Journal of Geophysical Research : Solid Earth*, 2020, 10.1029/2019JB018639 . hal-02867108

**HAL Id: hal-02867108**

**<https://hal.science/hal-02867108v1>**

Submitted on 23 Jun 2022

**HAL** is a multi-disciplinary open access archive for the deposit and dissemination of scientific research documents, whether they are published or not. The documents may come from teaching and research institutions in France or abroad, or from public or private research centers.

L'archive ouverte pluridisciplinaire **HAL**, est destinée au dépôt et à la diffusion de documents scientifiques de niveau recherche, publiés ou non, émanant des établissements d'enseignement et de recherche français ou étrangers, des laboratoires publics ou privés.

Copyright

# JGR Solid Earth

## RESEARCH ARTICLE

10.1029/2019JB018639

### Key Points:

- Magnetic scanning was firstly applied to a marine ferromanganese nodule, indicating growth rates of 4–5 mm/Myr
- Magnetic and chemical properties indicate the nodule may not roll over during its growing process and suggest a symmetric growth
- Magnetic signals recorded in the nodule can be well correlated to Earth's magnetic field changes

### Supporting Information:

- Supporting Information S1
- Supporting Information S2

### Correspondence to:

L. Yi, M. Medina-Elizalde, H. Yao and C. Deng,  
yiliang@tongji.edu.cn;  
mam0199@auburn.edu;  
hqyao@163.com;  
cldeng@mail.iggcas.ac.cn

### Citation:

Yi, L., Medina-Elizalde, M., Kletetschka, G., Yao, H., Simon, Q., Paterson, G. A., et al. (2020). The potential of marine ferromanganese nodules from Eastern Pacific as recorders of Earth's magnetic field changes during the past 4.7 Myr: A geochronological study by magnetic scanning and authigenic  $^{10}\text{Be}/^9\text{Be}$  dating. *Journal of Geophysical Research: Solid Earth*, 125, e2019JB018639. <https://doi.org/10.1029/2019JB018639>

Received 11 SEP 2019

Accepted 1 JUN 2020

Accepted article online 10 JUN 2020












### Author Contributions:

**Conceptualization:** L. Yi, J. Xiao, C. Deng

**Formal analysis:** L. Yi, M. Medina-Elizalde, G. Kletetschka, H. Yao, Q. Simon, G. A. Paterson, D. L. Bourlès, X. Deng, J. Du, H. Qin, Y. Chen, Q. Xie, J. Xiao, Y. Wang, C. Andreucci, G. Aumaitre, Y. Liu, H. Wang, Z. Shen, X. Gu, T. Smith, H. Dang, Z. Jian, T. Song, H. He, R. Zhu

**Methodology:** L. Yi, G. Kletetschka, Q. Simon, G. A. Paterson, D. L. Bourlès, (continued)

## The Potential of Marine Ferromanganese Nodules From Eastern Pacific as Recorders of Earth's Magnetic Field Changes During the Past 4.7 Myr: A Geochronological Study by Magnetic Scanning and Authigenic $^{10}\text{Be}/^9\text{Be}$ Dating

L. Yi<sup>1,2,3</sup> , M. Medina-Elizalde<sup>4</sup>, G. Kletetschka<sup>5,6,7</sup> , H. Yao<sup>3,8</sup>, Q. Simon<sup>9</sup> , G. A. Paterson<sup>10,11,12</sup> , D. L. Bourlès<sup>9</sup>, X. Deng<sup>3,8</sup>, J. Du<sup>13,14</sup>, H. Qin<sup>11,14,15</sup> , Y. Chen<sup>16</sup>, Q. Xie<sup>17</sup>, J. Xiao<sup>18</sup>, Y. Wang<sup>1</sup> , C. Andreucci<sup>19</sup>, K. Keddadouche<sup>9</sup> , G. Aumaitre<sup>9</sup>, Y. Liu<sup>3,8</sup>, H. Wang<sup>3,8</sup>, Z. Shen<sup>11,14,15</sup>, X. Gu<sup>11,14,15</sup>, T. Smith<sup>11,14,15</sup>, H. Dang<sup>1</sup>, Z. Jian<sup>1</sup> , T. Song<sup>13,14</sup>, H. He<sup>11,14,15</sup> , C. Deng<sup>11,14,15</sup> , and R. Zhu<sup>11,14,15</sup> 

<sup>1</sup>State Key Laboratory of Marine Geology, Tongji University, Shanghai, China, <sup>2</sup>Laboratory for Marine Geology, Pilot National Laboratory for Marine Science and Technology, Qingdao, China, <sup>3</sup>Key Laboratory of Marine Mineral Resources, Ministry of Natural Resources, Guangzhou Marine Geological Survey, Guangzhou, China, <sup>4</sup>Department of Geosciences, Auburn University, Auburn, AL, USA, <sup>5</sup>Institute of Geology, Academy of Sciences of the Czech Republic, Prague, Czech Republic, <sup>6</sup>Faculty of Science, Charles University in Prague, Prague, Czech Republic, <sup>7</sup>Department of Geology and Geophysics, University of Alaska Fairbanks, Fairbanks, AK, USA, <sup>8</sup>Southern Marine Science and Engineering Guangdong Laboratory (Guangzhou), Guangzhou, China, <sup>9</sup>CEREGE UM34, Aix Marseille University, CNRS, IRD, INRAE, Coll France, Aix-en-Provence, France, <sup>10</sup>Department of Earth, Ocean and Ecological Sciences, University of Liverpool, Liverpool, UK, <sup>11</sup>Institutions of Earth Science, Chinese Academy of Sciences, Beijing, China, <sup>12</sup>Key Laboratory of Earth and Planetary Physics, Institute of Geology and Geophysics, Chinese Academy of Sciences, Beijing, China, <sup>13</sup>Beijing Key Laboratory of Bioelectromagnetism, Institute of Electrical Engineering, Chinese Academy of Sciences, Beijing, China, <sup>14</sup>University of Chinese Academy of Sciences, Beijing, China, <sup>15</sup>State Key Laboratory of Lithospheric Evolution, Institute of Geology and Geophysics, Chinese Academy of Sciences, Beijing, China, <sup>16</sup>Key Laboratory of Engineering Oceanography, Second Institute of Oceanography, Hangzhou, China, <sup>17</sup>Institute of Deep-sea Science and Engineering, Chinese Academy of Sciences, Sanya, China, <sup>18</sup>School of Marine Science and Technology, Tianjin University, Tianjin, China, <sup>19</sup>Institut de Physique du Globe de Paris, Université Paris Diderot, Sorbonne Paris-Cité, UMR 7154 CNRS, Paris Cedex 05, France

**Abstract** The Clarion and Clipperton Fracture Zones in the Eastern Pacific are well known as a manganese nodule belt, which developed since the late Oligocene. The slow growth rate of these marine ferromanganese nodules implies that they have potentially recorded long-term environmental changes. To produce environmental records from these nodules, their chronology needs to be established first. In order to achieve this objective, many dating methods have been applied; however, due to relatively low-resolution temporal constraint, high-resolution environmental signals recorded in marine ferromanganese nodules have not been well documented yet. In this paper, we present a geochronological study based jointly on magnetic scanning and analyses of the authigenic beryllium isotopes (authigenic  $^{10}\text{Be}/^9\text{Be}$ ) and the cobalt (Co) flux of a marine ferromanganese nodule. Results lead to the following observations: (1) The growth of the studied nodule resulted from a combination of hydrogenetic and diagenetic processes, and (2) a total of 24 magnetozones is recognized for the studied nodule. Correlation to the geomagnetic polarity timescale suggests that chrons from C3n.2r to C1n were recorded in the nodule, implying that the growth of this nodule initiated ~4.70 Ma, which agrees well with the authigenic  $^{10}\text{Be}/^9\text{Be}$  and Co chronometers. Furthermore, a consistent pattern of broad paleomagnetic field variations was observed between the nodule's magnetic signal and the ocean-floor magnetic fields of the South Atlantic, confirming the validity of our growth model. Overall, our study highlights the potential of marine ferromanganese nodules from the Eastern Pacific as recorders of changes in Earth's magnetic field.

## 1. Introduction

The formation of marine ferromanganese crusts and nodules (MFCs and MFNs, respectively) on the deep-sea floor results from the migration of manganese and iron, from reducing to oxidizing environments (Glasby, 2006). Due to their continuous, but slow growth, usually less than 1 cm/Myr, MFCs and MFNs

X. Deng, J. Du, H. Qin, Y. Chen, J. Xiao,  
K. Keddadouche

**Writing - original draft:** L. Yi,

M. Medina-Elizalde, Q. Simon,

D. L. Bourlès, X. Deng, C. Deng

**Writing - review & editing:** L. Yi,

M. Medina-Elizalde, G. Kletetschka,

H. Yao, Q. Simon, G. A. Paterson,

D. L. Bourlès, X. Deng, J. Du, H. Qin,

Y. Chen, Q. Xie, J. Xiao, Y. Wang,

C. Andreucci, K. Keddadouche,

G. Aumaître, Y. Liu, H. Wang, Z. Shen,

X. Gu, T. Smith, H. Dang, Z. Jian,

T. Song, H. He, C. Deng, R. Zhu

record long-term environmental changes such as bottom-water evolution (van de Flierdt et al., 2004) and terrestrial dust supply (Banakar et al., 2003). The Clarion and Clipperton Fracture Zones (C-C Zones) in the Eastern Pacific, located to the north of the equatorial high bioproductivity zone (Antoine et al., 1996), are known as the “Manganese nodule belt” (Halbach et al., 1988). Since the late Oligocene, abyssal erosion has occurred on a large scale (Keller & Barron, 1983; Kennett & Watkins, 1975), and MFNs have developed in abundance (Glasby, 2006).

The application of dating methods such as U-Th series (Ku, 1976),  $^{10}\text{Be}/^9\text{Be}$  (Graham et al., 2004; Segl et al., 1984), Co flux into MFCs and MFNs (Puteanus & Halbach, 1988),  $^{87}\text{Sr}/^{86}\text{Sr}$  (Richter & Turekian, 1993), and  $^{187}\text{Os}/^{188}\text{Os}$  (Klemm et al., 2005) enables establishing preliminary long-term age models (tens of millions of years), with applications in chemical and mineralogical studies, or in the study of MFCs and MFNs as economic resources (e.g., Halbach et al., 2017; Hein et al., 2013; Hein et al., 2015; van de Flierdt et al., 2004; Wegorzewski & Kuhn, 2014). Extracting more detailed geological and paleoceanographic information from MFCs and MFNs needs high-resolution age models. Magnetic scanning offers such an opportunity for MFCs (Noguchi et al., 2017; Oda et al., 2011). This technique, however, has not been applied to MFNs yet, because of different growth patterns.

Here, we report a geochronological study in the C-C Zones (Figure 1), located in the Eastern Pacific Ocean, by magnetic and chemical scanning and authigenic beryllium isotopes (authigenic  $^{10}\text{Be}/^9\text{Be}$ ) analyses. High-resolution magnetic scanning was first conducted on an MFN sample, collected from the western part of the C-C Zones in 2013 by the Guangzhou Marine Geological Survey, China Geological Survey. Together with  $^{10}\text{Be}/^9\text{Be}$  dating, these magnetic results allow establishing a reliable geochronological framework, coherent with results from the cobalt (Co) chronometer. The derived MFN geochronology is consistent with variations of Earth's magnetic field recorded by magnetic anomalies in the South Atlantic seafloor, suggesting a close relationship between the MFN magnetic field and long-term changes in Earth's magnetic field.

## 2. Methods

### 2.1. The Studied Nodule

We studied a nodule that is 36 mm in length, brownish-black in color with a densely packed, laminated growth pattern. The studied MFN (10.05°N, 154.32°W, 5,050 m water depth) was collected in 2013 using a box corer on cruise DY125-27. The vertical direction of the sample was identified in the box corer and verified in the laboratory by its smoother surface at the top with some white and white-gray benthos. The studied MFN was cut into three pieces (Figure 1c) at the Institute of Geology and Geophysics, Chinese Academy of Sciences. The left piece was cut into six subsamples for demagnetization (i in Figure 1c), the right piece was cut into 14 subsamples for  $^{10}\text{Be}/^9\text{Be}$  measurements (iii in Figure 1c), and the middle part (ii in Figure 1c) was polished on one side for the chemical and magnetic scans (36 mm in length, 24 mm in width, and 5 mm in thickness; Figure 1d).

### 2.2. $^{10}\text{Be}/^9\text{Be}$ Measurement

The authigenic beryllium isotopes analyses were carried out at the CEREGE “Cosmogenic Nuclides National Laboratory” (LN2C, Aix-en-Provence in France). A total of 14 subsamples was pretreated according to the chemical procedure established by Bourlès et al. (1989) and revised by Simon, Thouveny, Bourlès, Nuttin, et al. (2016).

Authigenic  $^{10}\text{Be}$  and  $^9\text{Be}$  were extracted from 0.3–0.5 g of dry sample by soaking them in 10 ml of 0.04 M hydroxylamine ( $\text{NH}_2\text{OH}\cdot\text{HCl}$ ) in a 25% acetic acid leaching solution at  $95 \pm 5^\circ\text{C}$  for 7 hr. A 2 ml aliquot of the resulting leaching solution was sampled for the measurement of the natural  $^9\text{Be}$  concentration, which is used as a normalizer to minimize potential environmental disturbances of the  $^{10}\text{Be}$  signal (Bourlès et al., 1989). The remaining solution was spiked with 300  $\mu\text{l}$  of a 0.98039 mg/g  $^9\text{Be}$ -carrier solution before Be-purification by chromatography in order to accurately determine  $^{10}\text{Be}$  sample concentrations from the accelerator mass spectrometer measurements of  $^{10}\text{Be}/^9\text{Be}$  ratios. The natural authigenic  $^9\text{Be}$  concentrations were measured using a graphite-furnace Atomic Absorption Spectrophotometer with a double beam correction (Thermo Scientific ICE 3400®). The standard-addition method and the addition of a constant volume of  $\text{Mg}(\text{NO}_3)_2$  solution were used to eliminate the matrix effects during the absorption and to allow measurements near the detection limit. Authigenic  $^9\text{Be}$  sample concentrations vary around  $2.47 \pm 0.28 \times 10^{-3}$  mg/g.

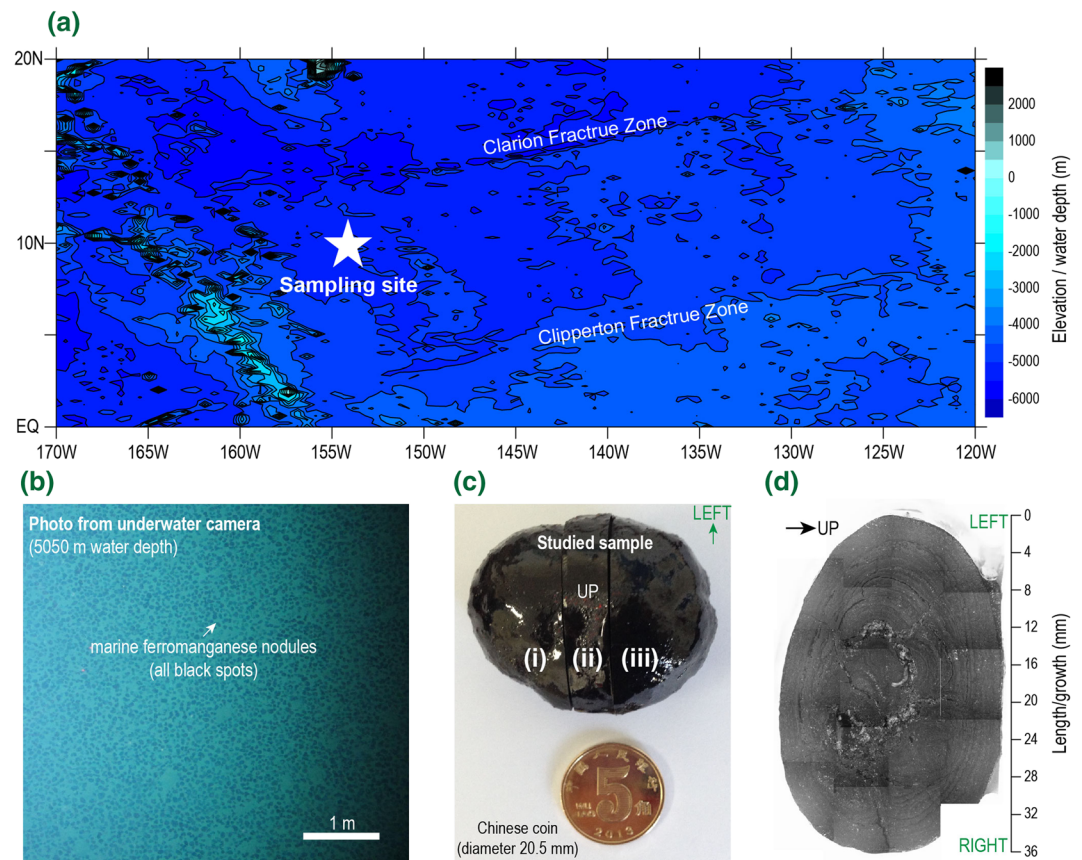


**Figure 1.** Map of the study location and the studied MFN. Bathymetric map of the Clarion and Clipperton Fracture Zones (C-C Zones) in the Eastern Pacific showing the study site (a). A photo taken by an underwater camera showing the distribution of MFNs on the seafloor at the study site (b). The studied MFN was cut into three pieces (i–iii) (c). The left piece (i) was prepared to obtain six 2 mm thick slices for stepwise demagnetization. The middle part (ii) was polished on one side for the chemical and magnetic scanning (d). The right piece (iii) was cut into 14 subsamples for  $^{10}\text{Be}/^9\text{Be}$  measurements.

The associated uncertainties ( $2\sigma$ ) based on the reproducibility of quadruplicated measurements and the least squares fitting between measured absorbance at each stage of the standard-addition method vary around average values of 1.9%.

Authigenic  $^{10}\text{Be}$  concentrations are calculated from the measured spiked  $^{10}\text{Be}/^9\text{Be}$  ratios normalized to the BeO STD-11 in-house standard ( $1.191 \pm 0.013 \times 10^{-11}$ ) (Braucher et al., 2015). The precision (from statistical and instrumental uncertainties) of the measured  $^{10}\text{Be}/^9\text{Be}$  ratios at the accelerator mass spectrometer has an average value of 1.7%. The uncertainties ( $2\sigma$ ) of the calculated Be-ratio are derived from analytical error propagation with an average value of 4.4%. All dating results are listed in supporting information Table S2.

### 2.3. Chemical Scanning

Chemical scanning was conducted at an 80  $\mu\text{m}$  interval through the studied MFN using an Electron Probe Microanalysis Jeol JXA-8100 with a wavelength dispersive spectrometer at the Institute of Geology and Geophysics, Chinese Academy of Sciences (36 mm length and 450 data points in total). The polished surface was first placed in a SC701C Quick Carbon Coater and coated with a carbon film. Prior to analysis, the thin sample was placed in the vacuum chamber of the electron-probe microanalyzer, and the air contained within the pores of the nodule was driven out using a vacuum pump. The accelerating voltage, beam current, and the diameter of the spots analyzed in this study were 20 kV,  $1 \times 10^{-8}$  A, and 50  $\mu\text{m}$ , respectively. Chemical elements were reported as weight percentage.

#### 2.4. Magnetic Scanning

Magnetic scanning was performed twice for the studied MFN using two types of instruments, namely, a room-temperature Hall probe and a low-temperature superconducting quantum interference device (SQUID). All measurements generate high-resolution maps of the vertical component of the sample magnetization field (Weiss et al., 2007), which can reflect microscale magnetic direction within the sample (Kletetschka et al., 2013; Oda et al., 2011). The room-temperature instrument consists of a stationary axial Hall probe with the sensor in a fiberglass tip sensor that is  $\sim 200 \mu\text{m}$  in size (Kletetschka et al., 2013). The movement stage was an automated 2-D motorized stage (Youngwood Science and Engineering, USA), with a spatial resolution of  $1 \mu\text{m}$ . The studied MFN was set in a magnetic shielding cylinder (diameter 12 cm; residual fields  $< 200 \text{ nT}$ ), and the measurements were completed at the Faculty of Science, Charles University in Prague, Czech Republic. Hall probe magnetic scanning without demagnetization was conducted at  $80 \mu\text{m}$  intervals and repeated 100 times along the same profile (the major measuring line) using a magnetic sensor, whose distance to the sample surface was 0.1 mm. Two additional profiles with parallel tracks to the major measuring line, with small offsets ( $\pm 80 \mu\text{m}$ ), were obtained by repeating 100 times to verify the magnetic signal. The background level was determined by measurements without the MFN specimen (repeated 100 times).

The SQUID microscope (gradiometer) is installed in a magnetically shielded room (residual fields  $< 150 \text{ nT}$ ) at the Beijing Key Laboratory of Bioelectromagnetism. Referring to the original design (Weiss et al., 2007), the instrument was modified in 2017 (Du et al., 2018), with an in situ magnetization (0–1 T)/demagnetization (0–300 mT, 400 Hz) function for the remanent magnetic field distribution and remanence curves. The gradiometer pick-up coils are 1 mm in diameter, vertically separated with each other at a distance of 2.6 mm, and have a sensor noise level of  $2.5 \times 10^{-10} \text{ T}/\sqrt{\text{Hz}}$ . The secondary magnetic scanning was performed for comparison on an area of  $2 \text{ mm} \times 36 \text{ mm}$  with a measuring interval of 0.1 mm in both width and length. The distance between the pick-up coil and the sample surface is 0.1 mm. The SQUID magnetic scanning was repeated 10 times, and 210 profiles were obtained. The final magnetic signal corresponds to the average of these repeated scans.

#### 2.5. Demagnetization

Six 2 mm thick slices were cut from one part of the studied MFN with a low-speed diamond wire-cutting machine (Model STX-202A). The wire diameter is 0.2 mm, and the slices were cut along the nodule growth axis with an area of  $\sim 4 \text{ mm} \times 3 \text{ mm}$ . These six slices were then subjected to stepwise alternating field demagnetization up to a peak field of 90 mT. The natural remanent magnetization of each slice was measured using a three-axis cryogenic magnetometer (2G Enterprise Model RAPID, USA) installed in a magnetically shielded room (residual fields  $< 300 \text{ nT}$ ). Characteristic remanent magnetization (ChRM) directions were determined using principal component analysis (PCA; Kirschvink, 1980) implemented by the PuffinPlot package (Lurcock & Wilson, 2012), with at least seven consecutive demagnetization steps and with a maximum angular deviation of less than  $5^\circ$ . In addition, various rock magnetic experiments were carried out to determine the magnetic minerals in the samples, and their results were detailed in the supporting information.

### 3. Results

#### 3.1. Chemical Properties and Cobased Chronology

The nodule contains  $27.7 \pm 7.4\%$  MnO (with a standard deviation, the same as follows),  $9.5 \pm 5.9\%$  FeO,  $1.3 \pm 0.7\%$  CuO,  $1.4 \pm 0.8\%$  NiO, and  $0.35 \pm 0.13\%$  CoO in average. The determined Mn/Fe ratio varies significantly around a median value of 2.8, with an interquartile range of 1.7–7.1. Observed Mn/Fe variability suggests that its growth resulted from a combination of hydrogenetic and diagenetic processes (Figure 2), as revealed by the observed relationship between Fe, Mn, and Ni + Co.

Regarding hydrogenetic MFNs and MFCs, there are four empirical formulae for Co flux: [growth rate =  $1.28 / (\text{Co} - 0.24)$ ] (Puteanus & Halbach, 1988), [growth rate =  $0.68 / (\text{Co})^{1.67}$ ] (Manheim & Lane-Bostwick, 1988), [growth rate =  $0.25 / (\text{Co})^{2.69}$ ] (Frank et al., 1999), and [growth rate =  $1.67 / (\text{Co})^{0.47}$ ] (McMurtry et al., 1994). Applying these four equations to chemical scanning data enables a rough chronological estimate for the studied MFN. To fit the equation of [growth rate =  $1.28 / (\text{Co} - 0.24)$ ] (Puteanus & Halbach, 1988), which was

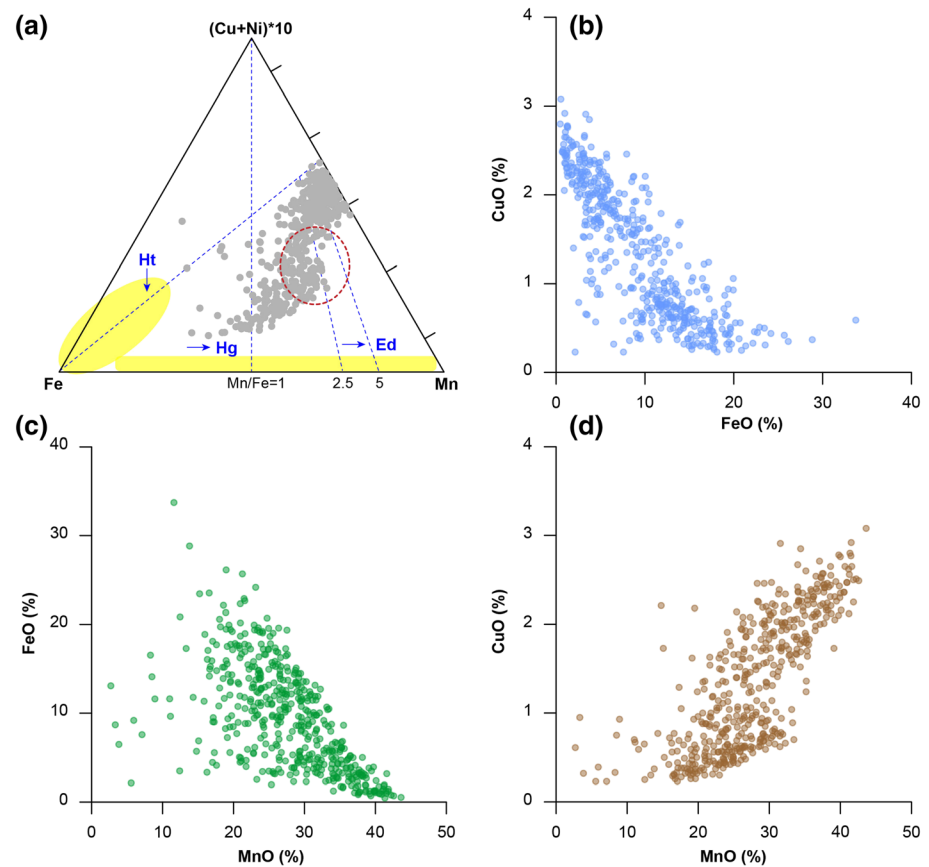


**Figure 2.** Chemical characteristics of the studied MFN. (a) Ternary diagram of Fe, Mn, and  $(\text{Cu} + \text{Ni}) \times 10$  following (Bonatti et al., 1972). The yellow-shaded area indicates the main influence of hydrothermal process, and other areas represent the dominance of hydrogenic and early diagenetic process. Samples with an Mn/Fn ratio above 2.5 (some refer to 5) indicate an increasing influence of early diagenetic process. Dashed circle labeled CCZ is from previously studied samples in the same area (Wegorzewski & Kuhn, 2014). (b–d) Relationships between metal elements. Ht = hydrothermal; Hg = hydrogenic; Ed = early diagenetic.

developed for Co-rich MFCs, low Co content data ( $<0.24\%$ ) were removed from the original record. As a result, eight growth rates were obtained (Figure 3a). The Co chronometer assumes that Co results from a hydrogenic process and that its flux in seawater is constant (Halbach et al., 1983; Manheim & Lane-Bostwick, 1988). Nevertheless, over several tens of million years, environmental conditions could have changed. For example, chemical properties of the studied MFN imply a combination of hydrogenic and diagenetic processes (Figure 2), likely implying that the relationship between Co flux and MFN growth rates varied with time. Although there are differences in estimated growth rates among the various methods applied (Joshima & Usui, 1998; Oda et al., 2011), the inferred initial ages of the MFNs and MFCs are broadly useful (Frank et al., 1999; Graham et al., 2004; Joshima & Usui, 1998; Klemm et al., 2005). The mean age at the center of the studied MFN (18.0 mm) was estimated as  $4.26 \pm 1.02$  Ma, based on the eight Co-derived ages (3.32, 3.36, 3.41, 3.54, 4.48, 4.48, 5.66, and 5.80 Ma), which is consistent with previously reported ages of MFNs from this region (Barash & Kruglikova, 2000).

### 3.2. $^{10}\text{Be}/^9\text{Be}$ -Based Chronology

The  $^{10}\text{Be}/^9\text{Be}$  ratios are generally stratigraphically consistent (Table S2) and can be well expressed with a logarithmic function ( $r = 0.99$ ,  $n = 14$ ,  $p < 0.01$ ; Figure 3b). This indicates that the growth pattern was relatively constant and suggests a closed system. Considering these aspects, the calculation of a radiometric  $^{10}\text{Be}/^9\text{Be}$ -based age model relies on an assumed age for a surface sample and the radioactive decay of the  $^{10}\text{Be}$  cosmogenic radionuclide progressively scavenged during growth (Bourlès et al., 1989). The calculations are listed as follows:

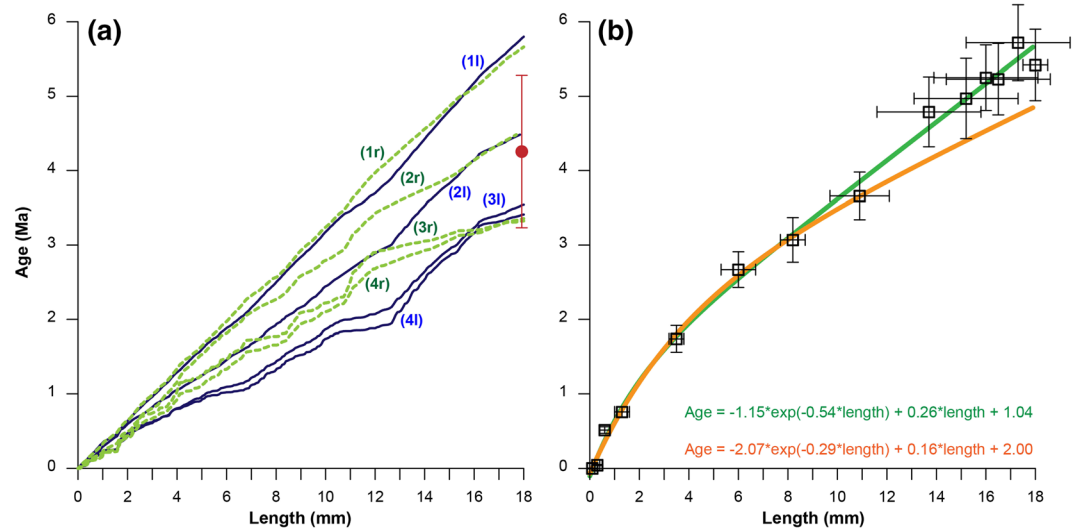


**Figure 3.** Ages of Co chromometer (a) and <sup>10</sup>Be/<sup>9</sup>Be dating (b). (1–4) in (a) represent estimates of Co chromometers of [growth rate = 1.28 / (Co content – 0.24)] (Puteanus & Halbach, 1988), [growth rate = 0.68 / (Co content)<sup>1.67</sup>] (Manheim & Lane-Bostwick, 1988), [growth rate = 0.25 / (Co content)<sup>2.69</sup>] (Frank et al., 1999), and [growth rate = 1.67 / (Co content)<sup>0.47</sup>] (McMurtry et al., 1994), respectively; and (r) and (l) represent right (dashed lines) and left (solid lines) sides of the studied MFN. Bold lines in (b) represent regressions of <sup>10</sup>Be/<sup>9</sup>Be-based ages versus their lengths. The green line is an age model fit to all ages, and the orange line is an age model fit to the first eight ages. See text for a discussion of these models.

$$t_i = -\frac{\ln\left(\frac{B_1}{B_i}\right)}{\lambda}; \lambda = \frac{\ln(2)}{1.387}$$

Here,  $B_i$  is the <sup>10</sup>Be/<sup>9</sup>Be value for the  $i$ th specimen, where  $i = 2$  to 14, the <sup>10</sup>Be half-life ( $T_{1/2}$ ) is  $1.387 \pm 0.012$  Ma (Chmeleff et al., 2010; Korschinek et al., 2010), and  $t_i$  is radiometric age, namely, the temporal span between the  $i$ th sample and the surface, assuming constant <sup>10</sup>Be production over the long time period averaged within each sample and that the age of the surface is the present ( $t_1 = 0$  Ma).

As a result, the paired age-length data from <sup>10</sup>Be/<sup>9</sup>Be dating exhibit a significantly negative exponential relationship ( $R^2 = 0.996$ ,  $n = 14$ ,  $F = 761$ ), reflecting a relatively continuous growing process (green curve in Figure 3b). This regression leads to an estimated age of  $5.42 \pm 0.34$  Ma for the center of the studied MFN. Notably, the <sup>10</sup>Be/<sup>9</sup>Be-based ages close to the center of the studied MFN overlap due to their associated large uncertainties, which may reflect three aspects of MFN formations. During the early stage of MFN growth in the C-C Zones, old MFNs (formed during the Oligocene and the Miocene) and their fragments could be an important polymetallic source for the formation of new MFNs (the Plio-Pleistocene) by (re)generation processes (Jeong et al., 1996). Moreover, because the structure of the left side is clearer than that on the right side close to the MFN center, there is a discrepancy in matching both sides, yielding interlayer contamination. In addition, there are two less-compacted layers within the intervals of 11–12 and 23–24 mm (stars in Figure 4a). These layers indicate a physical disturbance, which may have certain extensions to the MFN center that were included during sample preparation. All of these processes have probably induced slight <sup>10</sup>Be-depletion, resulting in age overestimation and inducing a wider dispersion and greater uncertainties. Thereby, a regression model based on the first eight ages was obtained (orange curve in Figure 3b). This model shows a significant relationship between the paired age-length data of the <sup>10</sup>Be/<sup>9</sup>Be chronology ( $R^2 = 0.997$ ,  $n = 8$ ,  $F = 386$ ). This regression model yields another estimated age of  $4.85 \pm 0.66$  Ma for the center of the studied MFN, which is similar, within uncertainties, to the Co-based age ( $4.26 \pm 1.02$  Ma), suggesting that this MFN developed since the early Pliocene.

### 3.3. Symmetric Growth of the Studied MFN

Usually, an MFN grows symmetrically and develops a ring/stratification structure (e.g., Benites et al., 2018; Glasby, 2006; Halbach et al., 1988; Halbach et al., 2017). This morphology implies that changes in chemical





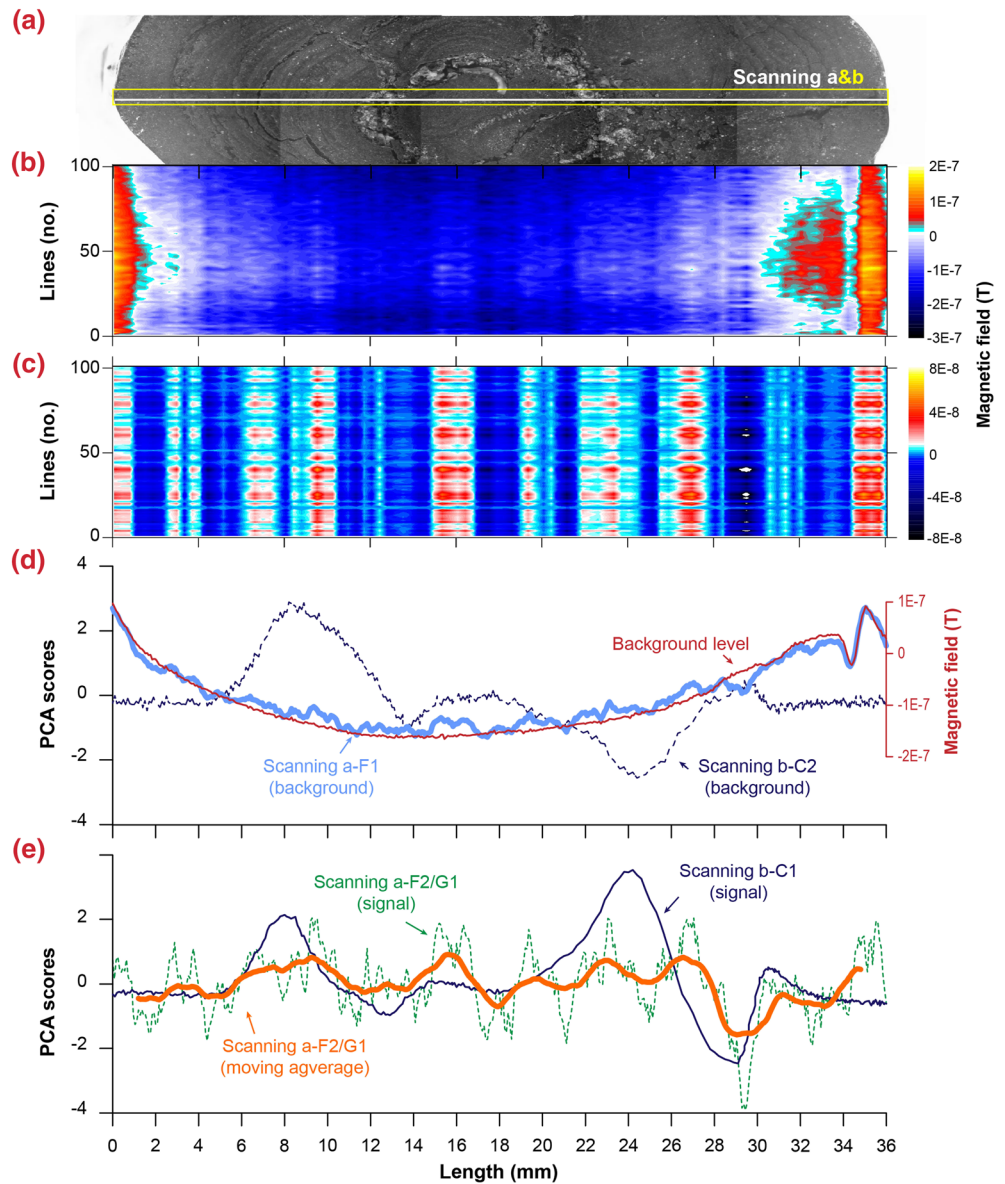


**Figure 5.** Comparison of magnetic signals by two types of magnetic scanning of the studied MFN. (a) Image of the sampled nodule marking out the measurement position for magnetic scanning. (b) Results of magnetic scanning using a stationary Hall probe, with the measurements repeated 100 times along the same measurement profile, labeled “scanning a” in (a). (c) Results of magnetic scanning after removing the background. (d) Comparison of the background changes of the two scanning methods using principal component analysis. (e) Comparison of changes in the magnetic field of the studied MFN from the two scanning methods. The bold line in (e) indicates the 31-point moving average. See the results in Table S2. Note that results in (c) were obtained by subtracting the background level (d) from the original 100 measurements (b).

with changes in the G1 (Figure 5e), while the secondary component (C2) only accounts for 16.1% of the total variance (Table S2) and could correspond to noise during scanning (Figure 5d). We then calculate an arithmetic mean of the detrended records of the 100 Hall-based scans (Figure 5c) to obtain the magnetic field variation of the studied MFN (Figure 6g). Rock magnetic analyses (Figure S3) indicate that magnetite is the main magnetic minerals with the studied MFN. These results therefore support high-stability and high-fidelity recording of geomagnetic field variation.

Further comparisons are performed using the ChRMs from alternating field demagnetization of six thin slices (Figures 6a–6f). The ChRMs generally match changes in magnetic field of the studied MFN

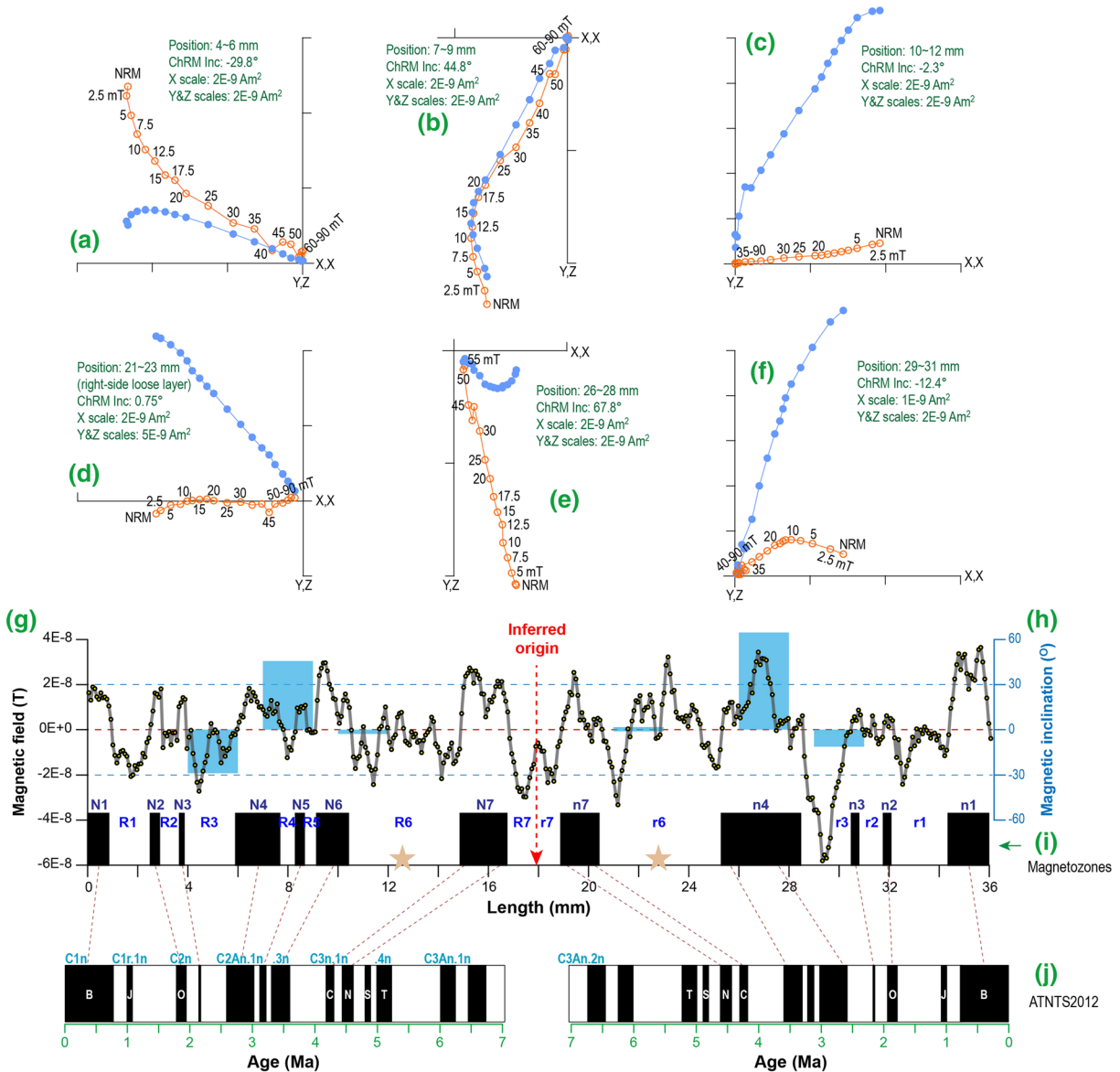


**Figure 6.** Orthogonal diagrams of progressive alternating field demagnetization for six thin slices and identified magnetozones based on results of magnetic scanning. (a–f) The solid (open) circles represent the horizontal (vertical) planes. AF demagnetization steps are 2.5, 5, 7.5, 10, 12.5, 15, 17.5, 20, 25, 30, 35, 40, 45, 50, 60, 70, 80, and 90 mT. The sample at 21–23 mm (d) was collected from the less-compact layer on the right side. NRM is the natural remanent magnetization, and the magnetic declinations are arbitrary. ChRM Inc is the inclination of characteristic remanent magnetization. (g and i) Magnetozones identified from magnetic scanning by the Hall probe (labeled N1–N7, R1–R7, n1–n7, and r1–r7). The magnetic signal of the studied MFN (g) is the mean of the data in Figure 5c. Uppercase and lowercase denote the left and right sides of the nodule, respectively. (h) ChRM inclination values of thin slices (blue rectangles). Two less compacted layers are labeled with stars in (i). (j) The ATNTS2012. B = Brunhes (C1n); J = Jaramillo (C1r.1n); O = Olduvai (C2n); C = Cochiti (C3n.1n); N = Nunivak (C3n.2n); S = Sidufall (C3n.3n); T = Thvera (C3n.4n). Dashed lines show possible correlations.

(Figures 6h–6g), and the magnetic declinations are arbitrary, indicating that high-resolution magnetic scanning can be used to obtain a magnetostratigraphic sequence. In addition, although the average value (26.3°,  $n = 6$ ) of the absolute inclinations (−29.8°, 44.8°, −2.3°, 0.75°, 67.8°, and −12.4°) is close to the present value in the study area (21° to 23°; <http://www.ngdc.noaa.gov/geomag/>), their large standard deviation (37.0°) may be attributed to discrepancy in matching layers and ring structures during thin-slice preparations. Thus, unlike the case of MFCs (Joshima & Usui, 1998; Oda et al., 2011), the only magnetostratigraphy of MFNs from demagnetizing a series of thin slices may not be appropriate to establish a chronology. Furthermore, considering that no abyssal storms, hyperpycnal flows, or sediment

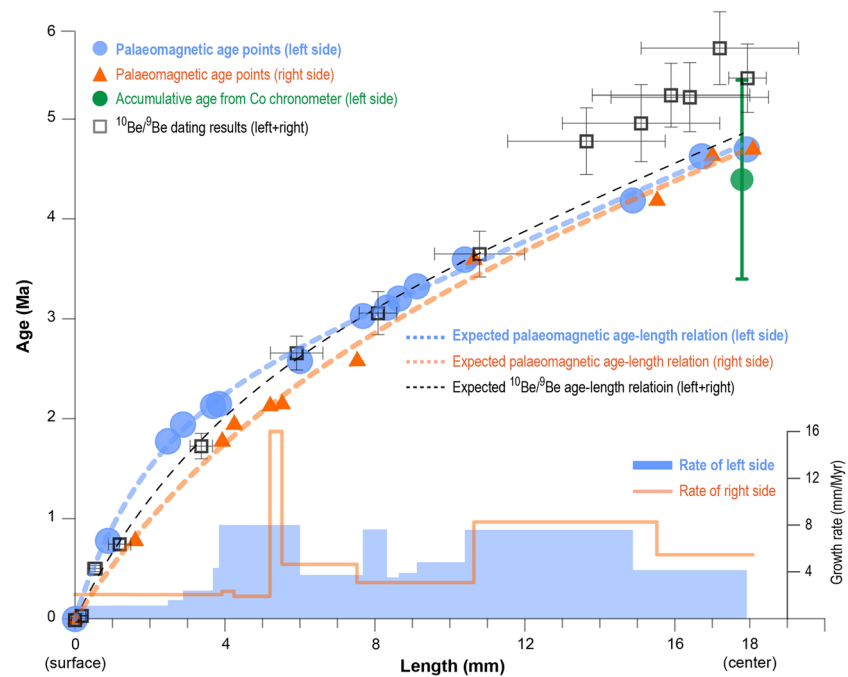


**Figure 7.** Age constraint and growth rate for the studied MFN. Four empirical formulae describing Co flux into MFNs provide a preliminary age estimate of  $5.02 \pm 1.07$  Ma for the center of the nodule (position 17.9 mm), which agrees with other MFNs from the same area (Barash & Kruglikova, 2000). The geochronological framework and growth rates were established by linear interpolation of paleomagnetic constraints. The paleomagnetic constraints from the left and right sides can be fitted as  $[AGE = -1.78 * \exp(-0.55 * length) + 0.17 * length + 1.78]$ ;  $AGE = -2.03 * \exp(-0.21 * length) + 0.15 * length + 2.03]$ , respectively. The  $^{10}\text{Be}/^9\text{Be}$  age constraints (the first eight data) average both sides (the orange line in Figure 3b). All parameters of the three formulas (dash lines) are significant at  $p < 0.1$  level with  $>99\%$  of the total variance explained, demonstrating continuous growth of the studied MFN and the consistency between paleomagnetic and  $^{10}\text{Be}/^9\text{Be}$  dating.

slumping was identified in the studied area (Jeong et al., 1996; Wang et al., 2014), together with the behavior of demagnetization, it is inferred that the nodule did not roll over during its growing process.

Due to growth symmetry, the two less compacted layers, likely reflecting coeval deposition, are taken as markers, and a total of 24 magnetozones is recognized, defined by at least four continuous magnetic (scanning) points of the Hall probe (Figure 6i). Within the two less compacted layers, although normally magnetized points can be observed on both sides from the repeated measurement profile, the less-compacted layer of the right side has more normal points, relative to the left side, reflecting a low-degree symmetry of changes in the magnetic field in this interval. Moreover, cobalt MFN contents within the two less-compacted layers,  $0.22 \pm 0.06\%$  and  $0.21 \pm 0.08\%$  for the right and left sides, respectively, are slightly lower than the average value of the entire sample ( $0.28 \pm 0.13\%$ ). Considering that the higher the growth rate, the lower the cobalt concentration (e.g., Puteanus & Halbach, 1988), these two less-compacted layers may indicate faster growth. Thereby, it is inferred that the normal points within these two layers may be “noise” produced during an interval of rapid growth and were not identified as magnetozones.

## 4. Discussion

### 4.1. Correlating MFN Magnetozones to the Astronomically Tuned Neogene Timescale (ATNTS2012)

As confirmed by the Co and  $^{10}\text{Be}/^9\text{Be}$  chronometers (Figure 3), MFNs in the C-C Zones have mainly developed during the Plio-Pleistocene (e.g., Barash & Kruglikova, 2000; Jeong et al., 1996). Based on this observation, the identified magnetozones of the studied MFN can be unambiguously correlated to the ATNTS2012 (Hilgen et al., 2012), inferring that chrons from C3n.2n to C1n were recorded in both left and right sides of the studied nodule (Figure 6). Specifically, 12 normal magnetozones (N1–N6 and n1–n6) can be correlated to the Brunhes chron (C1n), Olduvai chron (C2n), Reunion subchron (C2r.1n),

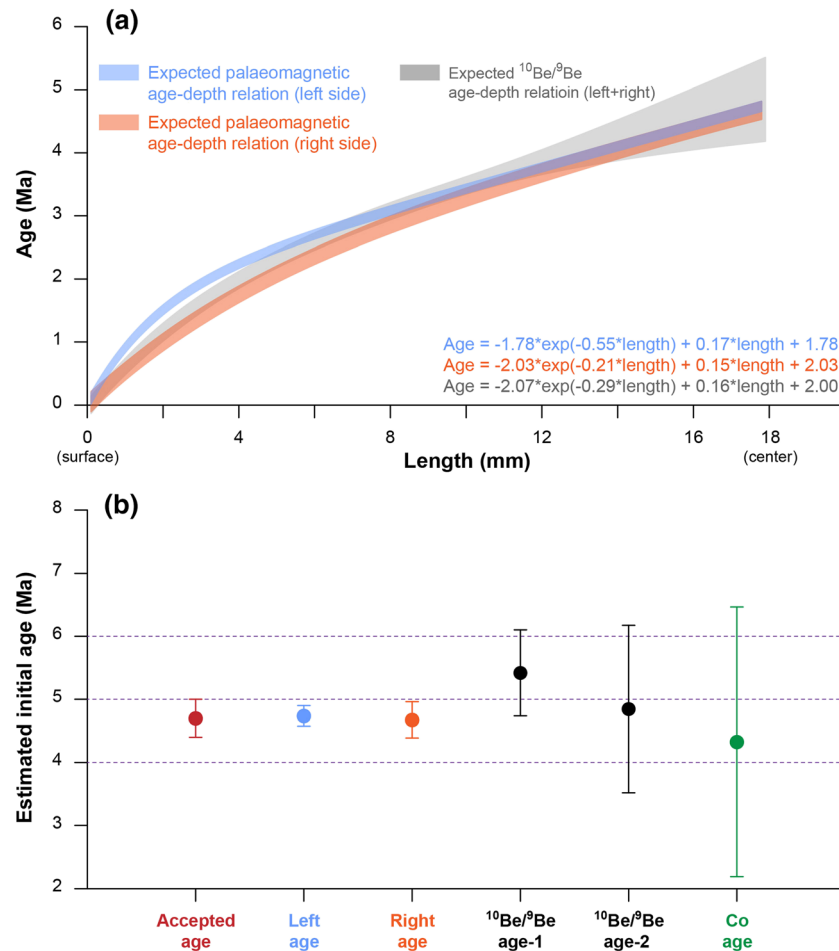


**Figure 8.** Comparisons between various expected ages. (a) Comparison between 95% confidence intervals of the expected age-length models by various methods. (b) Comparison between the estimated initial age (the center). The  $^{10}\text{Be}/^9\text{Be}$  age-length model in (a) was estimated using the first eight points (the orange line in Figure 3b). The accepted age,  $4.70 \pm 0.15$  Ma (1-sigma, same as follows); left and right ages,  $4.74 \pm 0.08$  and  $4.67 \pm 0.14$  Ma, respectively, determined by paleomagnetic scanning;  $^{10}\text{Be}/^9\text{Be}$  age-1,  $5.42 \pm 0.34$  Ma;  $^{10}\text{Be}/^9\text{Be}$  age-2,  $4.85 \pm 0.66$  Ma, estimated by the expected age-length models (Figure 3b); Co age,  $4.26 \pm 1.02$  Ma, determined by Co flux into MFNs. All the 95% confidence intervals (2-sigma, as plotted in (b)) of the five ages overlap, demonstrating the robustness of the initial age of the studied MFN.

Gauss chron (C2An), Cochiti subchron (C3n.1n), and Nunivak subchron (C3n.2n) (Table S3). Reversed magnetozones R1–R7 and r1–r7 can be correlated to the intervening Matuyama and Gilbert chrons, respectively. In addition, due to the presence of two less-compacted layers within the reversed magnetozones (R6 & r6), the normal magnetozones (N7 & n7) may have some other correlations to the ATNTS2012, such as Sidufjall subchron (C3n.3n), Thvera subchron (C3n.4n), or C3An chrons. However, cobalt concentration of the two less-compacted layers suggests a relatively rapid growth, and  $^{10}\text{Be}/^9\text{Be}$  dating infers possible age overestimation for the center area of the studied MFN. These lines of evidence lead to the correlations shown in Figure 6. The possibility of correlation with some older chrons/subchrons remains, but it must be justified with additional evidence.

Subsequently, linear interpolation of the paleomagnetic age constraints is used to estimate the growth rates of the left and right sides (Figure 7). This age model provides average growth rates of  $4.20 \pm 2.21$  and  $4.94 \pm 4.15$  mm/Myr for the left and right sides, respectively. The growth of the studied MFN is estimated to have started at  $4.70 \pm 0.15$  Ma (position 17.92 mm). To verify the reliability of the MFN geochronology, we compared all age constraints, the expected age-length relationship, and the expected starting growth age resulting from various dating methods (Figures 7 and 8).

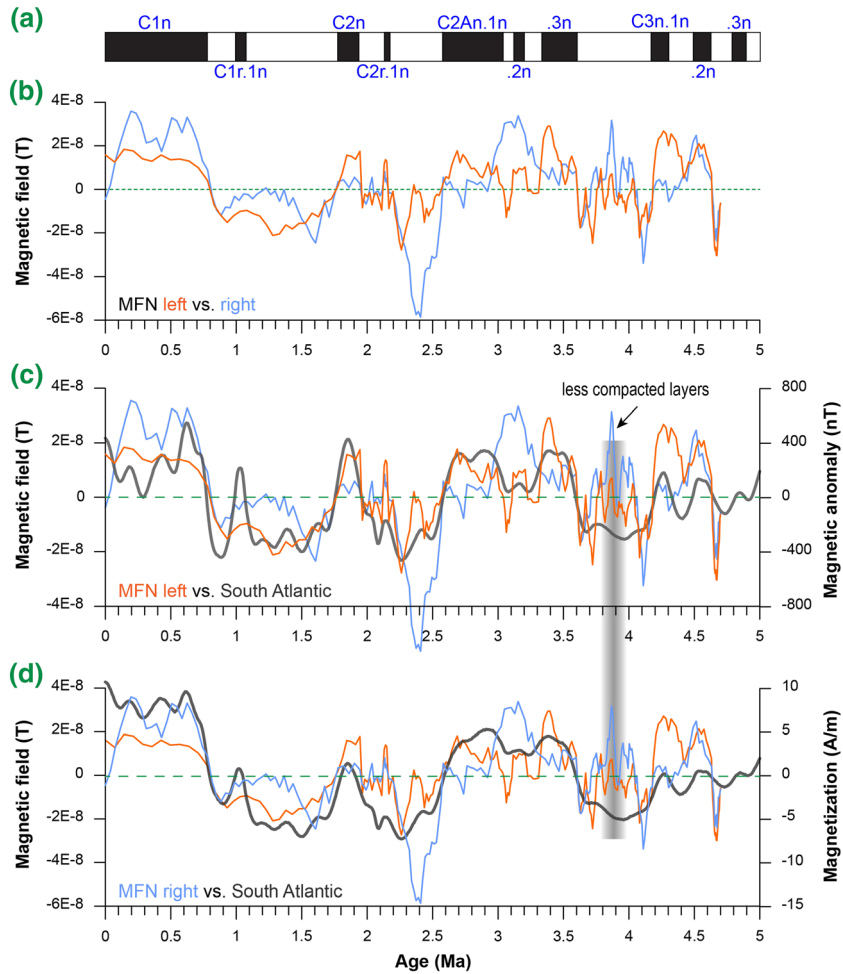


**Figure 9.** Comparison of the magnetic signal of the studied MFN with marine magnetic anomalies from the South Atlantic. (a) The ATNTS2012. (b) Comparison between magnetic fields of the left and right sides of the studied MFN. The magnetic signals of the studied MFN are the same as in Figure 6g and are placed on a timescale by linearly interpolating the pertinent paleomagnetic reversal ages. (c and d) Comparisons between magnetic field of the studied MFN and the seafloor magnetic anomaly and magnetization of the South Atlantic (Li et al., 2018).

Because samples used for  $^{10}\text{Be}/^9\text{Be}$  dating were cut from one half of the studied MFN, we must assume that age estimates are representative of both left and right sides. As shown, over the past 3.8 Ma,  $^{10}\text{Be}/^9\text{Be}$  ages agree well with the paleomagnetic ages and generally overlap with paleomagnetic age values of both sides (Figure 7). Prior to  $\sim 3.8$  Ma,  $^{10}\text{Be}/^9\text{Be}$  ages are somewhat overestimated, as noted above. Moreover, the paleomagnetic-based ages as a function of MFN length exhibit significantly negative exponential relationships on both sides, the left ( $R^2 = 0.998$ ,  $n = 8$ ,  $F = 1,772$ ) and the right ( $R^2 = 0.996$ ,  $n = 8$ ,  $F = 553$ ). Compared with the regression line of the  $^{10}\text{Be}/^9\text{Be}$ -based ages, all the expected age-length relationships are comparable, and the  $^{10}\text{Be}/^9\text{Be}$ -based regression line overlaps with those based on paleomagnetic ages (Figure 8a). This consistency between  $^{10}\text{Be}/^9\text{Be}$ - and paleomagnetic-based chronologies, in addition to the observed overlap of all expected ages for the MFN center (CI 95%) based on the various dating methods, offers strong support to the derived chronology of this particular MFN (Figure 8b).

#### 4.2. Linking MFN Magnetic Signals to Changes in the Earth's Magnetic Field Intensity

How the Earth's magnetic field intensity changes is a critical question for understanding the past, the present, and the future of geodynamo regimes (Hulot et al., 2010). Due to the relatively short periods of direct observation, geological investigations of sediments and lavas can provide information on long-term variations of the dipole field (e.g., Cai et al., 2017; Channell et al., 2009; Guyodo & Valet, 1999; Simon, Thouveny, Bourlès, Nuttin, et al., 2016; Tauxe, 1993; Valet et al., 2005). Specifically, the absolute, but

scattered, paleointensity reconstructed from lava records can be used to model virtual axial dipole moment (e.g., Cai et al., 2017), while relative paleointensity reconstructed from sedimentary records can produce long-term and continuous global stacks to significantly extend our understanding of changes in the Earth's magnetic field intensity (e.g., Channell et al., 2016). Sediment-based reconstructions of paleointensity, however, remain challenging, and discrepancies are observed between absolute and relative intensity information, which may be introduced by remanent magnetization acquisition during depositional and postdepositional processes (e.g., Roberts et al., 2013; Tauxe et al., 2006; Valet & Fournier, 2016).

To overcome this problem and further extend paleointensity records to the distant past, different studied materials and/or proxies of Earth's magnetic field intensity have been offered. For instance, authigenic  $^{10}\text{Be}/^9\text{Be}$  ratio can be measured together with paleomagnetic analyses to propose independent estimates and/or to correct potential biases on relative paleointensity (e.g., Simon, Thouveny, Bourlès, Valet, et al., 2016; Simon et al., 2018). Records of Earth's magnetic field intensity can be extracted from seafloor magnetic anomalies (Gee et al., 2000; Li et al., 2018). In this study, based on the reliable geochronology of the studied MFN, we compared the magnetic signal obtained from magnetic scans with changes on seafloor magnetic anomalies in the South Atlantic (Figure 9). Highly correlated magnetic field records between the left and right sides strengthen the symmetric growth of the studied MFN (Figure 9b). Comparisons between the MFN magnetic record and oceanic-floor magnetic anomalies and magnetization from the South Atlantic reveal a consistent pattern of broad paleomagnetic field variations (Figures 9c and 9d). A similar relationship can be observed in an attempt of magnetic scanning of MFCs collected from the Northwest Pacific (Oda et al., 2011). In addition, high-frequency changes in Earth's magnetic field of the studied MFN prior to 1.5 Ma are evident, and even some subchrons, such as C2r.1n and C2A.2n, can be identified, suggesting a greater MFN capacity for recording changes in Earth's magnetic field during intervals with high growth rates. The results of this study suggest that MFNs from Eastern Pacific can record the Earth's magnetic field and that their remanence carriers and remanent magnetization acquisition is a matter of significant interest and worth of rigorous examination.

## 5. Conclusions

This study presents the chronology of a MFN (36 mm in length) collected from the C-C Zones of the Eastern Pacific, based on high-resolution magnetic and chemical scanning, combined with authigenic  $^{10}\text{Be}/^9\text{Be}$  dating. The main findings of this study are that (1) the growth of the MFN resulted from a combination of hydrogenetic and diagenetic processes in the C-C Zones, (2) the 24 magnetozones identified in the studied nodule can be correlated from chron C1n down to chron C3n.2n, and (3) the magnetic based age model cross-correlates with authigenic  $^{10}\text{Be}/^9\text{Be}$ - and Co-based chronologies. They all suggest that the MFN was started to form at ~4.70 Ma. A good agreement was found between the MFN magnetic record and changes in Earth's magnetic field intensity derived from seafloor magnetic anomalies in the South Atlantic. Results from this study highlight the significant potential of MFNs from the Eastern Pacific to record changes in Earth's magnetic field intensity over millions of years.

## Data Availability Statement

Data sets including all magnetic and chemical scanning data were stored in an online repository "Marine Data Archive" ([https://mda.vliz.be/directlink.php?fid=VLIZ\\_00000824\\_5e54f74a50c01527278753](https://mda.vliz.be/directlink.php?fid=VLIZ_00000824_5e54f74a50c01527278753)).

## References

- Antoine, D., André, J.-M., & Morel, A. (1996). Oceanic primary production: 2. Estimation at global scale from satellite (coastal zone color scanner) chlorophyll. *Global Biogeochemical Cycles*, *10*(1), 57–69. <https://doi.org/10.1029/95gb02832>
- Banakar, V. K., Galy, A., Sukumaran, N. P., Parthiban, G., & Volvaiker, A. Y. (2003). Himalayan sedimentary pulses recorded by silicate detritus within a ferromanganese crust from the Central Indian Ocean. *Earth and Planetary Science Letters*, *205*(3–4), 337–348. [https://doi.org/10.1016/S0012-821X\(02\)01062-2](https://doi.org/10.1016/S0012-821X(02)01062-2)
- Barash, M. S., & Kruglikova, S. B. (2000). Age of manganese nodules of the Clarion-Clipperton Province and the problem of nodule maintenance at the sediment surface. In *PACON 99 Proceedings, Symposium on Humanity and the World Ocean: Interdependence at the Dawn of the New Millennium*, edited, (pp. 220–230). Honolulu, HI: PACON International.
- Benites, M., Millo, C., Hein, J., Nath, B., Murton, B., Galante, D., & Jovane, L. (2018). Integrated geochemical and morphological data provide insights into the genesis of ferromanganese nodules. *Minerals*, *8*(11), 488. <https://doi.org/10.3390/min8110488>

## Acknowledgments

The authors thank the Captain and crew onboard R/V HAI YANG LIU HAO on cruise DY125-27 and Dr. Mark J. Dekkers (Associate Editor) and two anonymous reviewers for their suggestions and comments in improving this manuscript. This research was supported by the National Natural Science Foundation of China (41888101, 41574063, 41425013, and 41690112), National Key R&D Program of China (2018YFE0202401), COMRA Project from China Ocean Mineral Resources R&D Association (DY135-C1-1-02, DY135-C1-1-01, and DY135-E2-1-01), and National Natural Science Foundation of Shanghai (19ZR1459800), and G. K. was supported by grants CGA 20-08294S, 20-00892 L, MEYS LTAUSA 19141, and RVO 67985831. The ASTER AMS national facility (D. B., K. K., and G.A.) was supported by the INSU/CNRS, the ANR through the "Projets thématiques d'excellence" program for the "Equipements d'excellence" ASTER-CEREGE action and IRD, and G. A. P. was further supported by Natural Environmental Research Council Independent Research Fellowship (NE/P017266/1).

- Bonatti, E., Kraemer, T., & Rydell, H. (1972). Classification and genesis of submarine iron-manganese deposits. In D. R. Horn (Ed.), *Ferromanganese deposits on the ocean floor*, (pp. 149–166). US, Washington D.C.: NSF.
- Bourlès, D., Raisbeck, G. M., & Yiou, F. (1989).  $^{10}\text{Be}$  and  $^9\text{Be}$  in marine sediments and their potential for dating. *Geochimica et Cosmochimica Acta*, 53(2), 443–452. [https://doi.org/10.1016/0016-7037\(89\)90395-5](https://doi.org/10.1016/0016-7037(89)90395-5)
- Braucher, R., Guillou, V., Bourlès, D. L., Arnold, M., Aumaître, G., Keddadouche, K., & Nottoli, E. (2015). Preparation of ASTER in-house  $^{10}\text{Be}/^9\text{Be}$  standard solutions. *Nuclear Instruments and Methods in Physics Research Section B: Beam Interactions with Materials and Atoms*, 361, 335–340. <https://doi.org/10.1016/j.nimb.2015.06.012>
- Cai, S., Jin, G., Tauxe, L., Deng, C., Qin, H., Pan, Y., & Zhu, R. (2017). Archaeointensity results spanning the past 6 kiloyears from eastern China and implications for extreme behaviors of the geomagnetic field. *Proceedings of the National Academy of Sciences*, 114(1), 39–44. <https://doi.org/10.1073/pnas.1616976114>
- Channell, J. E. T., Hodell, D. A., & Curtis, J. H. (2016). Relative paleointensity (RPI) and oxygen isotope stratigraphy at IODP Site U1308: North Atlantic RPI stack for 1.2–2.2 Ma (NARPI-2200) and age of the Olduvai Subchron. *Quaternary Science Reviews*, 131, 1–19. <https://doi.org/10.1016/j.quascirev.2015.10.011>
- Channell, J. E. T., Xuan, C., & Hodell, D. A. (2009). Stacking paleointensity and oxygen isotope data for the last 1.5 Myr (PISO-1500). *Earth and Planetary Science Letters*, 283(1-4), 14–23. <https://doi.org/10.1016/j.epsl.2009.03.012>
- Chmeleff, J., von Blanckenburg, F., Kossert, K., & Jakob, D. (2010). Determination of the  $^{10}\text{Be}$  half-life by multicollector ICP-MS and liquid scintillation counting. *Nuclear Instruments and Methods in Physics Research Section B: Beam Interactions with Materials and Atoms*, 268(2), 192–199. <https://doi.org/10.1016/j.nimb.2009.09.012>
- Du, J., Liu, X., Qin, H., Wei, Z., Kong, X., Liu, Q., & Song, T. (2018). Scanning SQUID microscope with an in-situ magnetization/demagnetization field for geological samples. *Physica C: Superconductivity and Its Applications*, 547, 1–6. <https://doi.org/10.1016/j.physc.2018.01.014>
- Frank, M., O'Nions, R. K., Hein, J. R., & Banakar, V. K. (1999). 60 Myr records of major elements and Pb–Nd isotopes from hydrogenous ferromanganese crusts: Reconstruction of seawater paleochemistry. *Geochimica et Cosmochimica Acta*, 63(11-12), 1689–1708. [https://doi.org/10.1016/S0016-7037\(99\)00079-4](https://doi.org/10.1016/S0016-7037(99)00079-4)
- Gee, J. S., Cande, S. C., Hildebrand, J. A., Donnelly, K., & Parker, R. L. (2000). Geomagnetic intensity variations over the past 780 kyr obtained from near-seafloor magnetic anomalies. *Nature*, 408(6814), 827–832. <https://doi.org/10.1038/35048513>
- Glasby, G. P. (2006). Manganese: Predominant role of nodules and crusts. In H. D. Schulz, & M. Zabel (Eds.), *Marine geochemistry*, (pp. 371–427). Berlin, Heidelberg: Springer Berlin Heidelberg. [https://doi.org/10.1007/3-540-32144-6\\_11](https://doi.org/10.1007/3-540-32144-6_11)
- Graham, I. J., Carter, R. M., Ditchburn, R. G., & Zondervan, A. (2004). Chronostratigraphy of ODP 181, Site 1121 sediment core (Southwest Pacific Ocean), using  $^{10}\text{Be}/^9\text{Be}$  dating of entrapped ferromanganese nodules. *Marine Geology*, 205(1-4), 227–247. [https://doi.org/10.1016/S0025-3227\(04\)00025-8](https://doi.org/10.1016/S0025-3227(04)00025-8)
- Guyodo, Y., & Valet, J.-P. (1999). Global changes in intensity of the Earth's magnetic field during the past 800 kyr. *Nature*, 399(6733), 249–252. <https://doi.org/10.1038/20420>
- Halbach, P. E., Friedrich, G., & von Stackelberg, U. (1988). The manganese nodule belt of the Pacific Ocean. In *Geological environment, nodule formation, and mining aspects*, (1–254). Stuttgart: Ferdinand Enke Verlag.
- Halbach, P. E., Jahn, A., & Cherkashov, G. (2017). Marine co-rich ferromanganese crust deposits: Description and formation, occurrences and distribution, estimated world-wide resources. In R. Sharma (Ed.), *Deep-sea mining: Resource potential, technical and environmental considerations*, (pp. 65–141). Cham: Springer International Publishing. [https://doi.org/10.1007/978-3-319-52557-0\\_3](https://doi.org/10.1007/978-3-319-52557-0_3)
- Halbach, P. E., Segl, M., Puteanus, D., & Mangini, A. (1983). Co-fluxes and growth rates in ferromanganese deposits from Central Pacific seamount areas. *Nature*, 304(5928), 716–719. <https://doi.org/10.1038/304716a0>
- Hein, J. R., Mizell, K., Koschinsky, A., & Conrad, T. A. (2013). Deep-ocean mineral deposits as a source of critical metals for high- and green-technology applications: Comparison with land-based resources. *Ore Geology Reviews*, 51(Supplement C), 1–14. <https://doi.org/10.1016/j.oregeorev.2012.12.001>
- Hein, J. R., Spinardi, F., Okamoto, N., Mizell, K., Thorburn, D., & Tawake, A. (2015). Critical metals in manganese nodules from the Cook Islands EEZ, abundances and distributions. *Ore Geology Reviews*, 68(Supplement C), 97–116. <https://doi.org/10.1016/j.oregeorev.2014.12.011>
- Hilgen, F. J., Lourens, L. J., & Van Dam, J. A. (2012). The Neogene period. In Gradstein F. M., Ogg J. G., Schmitz M. D., & Ogg G. M. (Eds.), *The geological time scale 2012*, (pp. 923–978). The Netherlands: Elsevier BV.
- Hulot, G., Finlay, C. C., Constable, C. G., Olsen, N., & Manda, M. (2010). The magnetic field of planet Earth. *Space Science Reviews*, 152(1-4), 159–222. <https://doi.org/10.1007/s11214-010-9644-0>
- Jeong, K. S., Kang, J. K., Lee, K. Y., Jung, H. S., Chi, S. B., & Ahn, S. J. (1996). Formation and distribution of manganese nodule deposit in the northwestern margin of Clarion-Clipperton fracture zones, northeast equatorial Pacific. *Geo-Marine Letters*, 16(2), 123–131. <https://doi.org/10.1007/bf02202607>
- Joshima, M., & Usui, A. (1998). Magnetostratigraphy of hydrogenetic manganese crusts from Northwestern Pacific seamounts. *Marine Geology*, 146(1-4), 53–62. [https://doi.org/10.1016/S0025-3227\(97\)00131-X](https://doi.org/10.1016/S0025-3227(97)00131-X)
- Keller, G., & Barron, J. A. (1983). Paleoceanographic implications of Miocene deep-sea hiatuses. *Geological Society of America Bulletin*, 94(5), 590–613. [https://doi.org/10.1130/0016-7606\(1983\)94<590:piomdh>2.0.co;2](https://doi.org/10.1130/0016-7606(1983)94<590:piomdh>2.0.co;2)
- Kennett, J. P., & Watkins, N. D. (1975). Deep-sea erosion and manganese nodule development in the Southeast Indian Ocean. *Science*, 188(4192), 1011–1013. <https://doi.org/10.1126/science.188.4192.1011>
- Kirschvink, J. L. (1980). The least-squares line and plane and the analysis of palaeomagnetic data. *Geophysical Journal of the Royal Astronomical Society*, 62(3), 699–718. <https://doi.org/10.1111/j.1365-246X.1980.tb02601.x>
- Klemm, V., Levasseur, S., Frank, M., Hein, J. R., & Halliday, A. N. (2005). Osmium isotope stratigraphy of a marine ferromanganese crust. *Earth and Planetary Science Letters*, 238(1-2), 42–48. <https://doi.org/10.1016/j.epsl.2005.07.016>
- Kletetschka, G., Schnabl, P., Šifnerová, K., Tasáryová, Z., Manda, Š., & Pruner, P. (2013). Magnetic scanning and interpretation of paleomagnetic data from Prague Synform's volcanics. *Studia Geophysica et Geodaetica*, 57(1), 103–117. <https://doi.org/10.1007/s11200-012-0723-4>
- Korschinek, G., Bergmaier, A., Faestermann, T., Gerstmann, U. C., Knie, K., Rugel, G., et al. (2010). A new value for the half-life of  $^{10}\text{Be}$  by heavy-ion elastic recoil detection and liquid scintillation counting. *Nuclear Instruments and Methods in Physics Research Section B: Beam Interactions with Materials and Atoms*, 268(2), 187–191. <https://doi.org/10.1016/j.nimb.2009.09.020>
- Ku, T. L. (1976). The uranium-series methods of age determination. *Annual Review of Earth and Planetary Sciences*, 4(1), 347–379. <https://doi.org/10.1146/annurev.ea.04.050176.002023>

- Li, Y., Liu, Q.-S., Wei, D., Li, S., & Yu, Y. (2018). Variations of earth magnetic field intensity for the past 5 Myr derived from marine magnetic anomalies in a slowly spreading South Atlantic ridge. *Journal of Geophysical Research: Solid Earth*, *123*, 7321–7337. <https://doi.org/10.1029/2018JB016099>
- Lurcock, P. C., & Wilson, G. S. (2012). PuffinPlot: A versatile, user-friendly program for paleomagnetic analysis. *Geochemistry, Geophysics, Geosystems*, *13*, Q06Z45. <https://doi.org/10.1029/2012gc004098>
- Manheim, F. T., & Lane-Bostwick, C. M. (1988). Cobalt in ferromanganese crusts as a monitor of hydrothermal discharge on the Pacific Sea floor. *Nature*, *335*(6185), 59–62. <https://doi.org/10.1038/335059a0>
- McMurtry, G. M., VonderHaar, D. L., Eisenhauer, A., Mahoney, J. J., & Yeh, H. W. (1994). Cenozoic accumulation history of a Pacific ferromanganese crust. *Earth and Planetary Science Letters*, *125*(1-4), 105–118. [https://doi.org/10.1016/0012-821X\(94\)90209-7](https://doi.org/10.1016/0012-821X(94)90209-7)
- Noguchi, A., Oda, H., Yamamoto, Y., Usui, A., Sato, M., & Kawai, J. (2017). Scanning SQUID microscopy of a ferromanganese crust from the northwestern Pacific: Submillimeter scale magnetostratigraphy as a new tool for age determination and mapping of environmental magnetic parameters. *Geophysical Research Letters*, *44*, 5360–5367. <https://doi.org/10.1002/2017gl073201>
- Oda, H., Usui, A., Miyagi, I., Joshima, M., Weiss, B. P., Shantz, C., et al. (2011). Ultrafine-scale magnetostratigraphy of marine ferromanganese crust. *Geology*, *39*(3), 227–230. <https://doi.org/10.1130/g31610.1>
- Puteanus, D., & Halbach, P. (1988). Correlation of Co concentration and growth rate—A method for age determination of ferromanganese crusts. *Chemical Geology*, *69*(1-2), 73–85. [https://doi.org/10.1016/0009-2541\(88\)90159-3](https://doi.org/10.1016/0009-2541(88)90159-3)
- Richter, F. M., & Turekian, K. K. (1993). Simple models for the geochemical response of the ocean to climatic and tectonic forcing. *Earth and Planetary Science Letters*, *119*(1-2), 121–131. [https://doi.org/10.1016/0012-821X\(93\)90010-7](https://doi.org/10.1016/0012-821X(93)90010-7)
- Roberts, A. P., Tauxe, L., & Heslop, D. (2013). Magnetic paleointensity stratigraphy and high-resolution quaternary geochronology: Successes and future challenges. *Quaternary Science Reviews*, *61*, 1–16. <https://doi.org/10.1016/j.quascirev.2012.10.036>
- Segl, M., Mangini, A., Bonani, G., Hofmann, H. J., Nessi, M., Suter, M., et al. (1984).  $^{10}\text{Be}$ -dating of a manganese crust from central North Pacific and implications for ocean palaeocirculation. *Nature*, *309*(5968), 540–543. <https://doi.org/10.1038/309540a0>
- Simon, Q., Bourlès, D. L., Thouveny, N., Horng, C.-S., Valet, J.-P., Bassinot, F., & Choy, S. (2018). Cosmogenic signature of geomagnetic reversals and excursions from the Réunion event to the Matuyama–Brunhes transition (0.7–2.14 Ma interval). *Earth and Planetary Science Letters*, *482*, 510–524. <https://doi.org/10.1016/j.epsl.2017.11.021>
- Simon, Q., Thouveny, N., Bourlès, D. L., Nuttin, L., Hillaire-Marcel, C., & St-Onge, G. (2016a). Authigenic  $^{10}\text{Be}/^9\text{Be}$  ratios and  $^{10}\text{Be}$ -fluxes ( $^{230}\text{Th}_{\text{xs}}$ -normalized) in central Baffin Bay sediments during the last glacial cycle: Paleoenvironmental implications. *Quaternary Science Reviews*, *140*, 142–162. <https://doi.org/10.1016/j.quascirev.2016.03.027>
- Simon, Q., Thouveny, N., Bourlès, D. L., Valet, J.-P., Bassinot, F., Ménabréaz, L., et al. (2016b). Authigenic  $^{10}\text{Be}/^9\text{Be}$  ratio signatures of the cosmogenic nuclide production linked to geomagnetic dipole moment variation since the Brunhes/Matuyama boundary. *Journal of Geophysical Research: Solid Earth*, *121*, 7716–7741. <https://doi.org/10.1002/2016jb013335>
- Tauxe, L. (1993). Sedimentary records of relative paleointensity of the geomagnetic field: Theory and practice. *Reviews of Geophysics*, *31*(3), 319–354. <https://doi.org/10.1029/93rg01771>
- Tauxe, L., Steindorf, J. L., & Harris, A. (2006). Depositional remanent magnetization: Toward an improved theoretical and experimental foundation. *Earth and Planetary Science Letters*, *244*(3-4), 515–529. <https://doi.org/10.1016/j.epsl.2006.02.003>
- Valet, J.-P., & Fournier, A. (2016). Deciphering records of geomagnetic reversals. *Reviews of Geophysics*, *54*, 410–446. <https://doi.org/10.1002/2015rg000506>
- Valet, J.-P., Meynadier, L., & Guyodo, Y. (2005). Geomagnetic dipole strength and reversal rate over the past two million years. *Nature*, *435*(7043), 802–805. <https://doi.org/10.1038/nature03674>
- van de Fliert, T., Frank, M., Halliday, A. N., Hein, J. R., Hattendorf, B., Günther, D., & Kubik, P. W. (2004). Deep and bottom water export from the Southern Ocean to the Pacific over the past 38 million years. *Paleoceanography*, *19*, P1020. <https://doi.org/10.1029/2003pa000923>
- Wang, H., Han, Y., Zhu, K., Yi, L., Deng, X., Liu, G., & Ren, J. (2014). A preliminary study on magnetostratigraphy and sedimentary evolution of piston core WPC1101 from Clarion-Clipperton Fracture zones, Eastern Pacific. *Journal of Jilin University (Earth Science Edition)*, *44*(6), 1892–1905. <https://doi.org/10.13278/j.cnki.jjuese.201406115>
- Wegorzewski, A. V., & Kuhn, T. (2014). The influence of suboxic diagenesis on the formation of manganese nodules in the Clarion Clipperton Nodule Belt of the Pacific Ocean. *Marine Geology*, *357*(Supplement C), 123–138. <https://doi.org/10.1016/j.margeo.2014.07.004>
- Weiss, B. P., Lima, E. A., Fong, L. E., & Baudenbacher, F. J. (2007). Paleomagnetic analysis using SQUID microscopy. *Journal of Geophysical Research*, *112*, B09105. <https://doi.org/10.1029/2007jb004940>